








# Fabrication and transfer printing based integration of free-standing GaN membrane micro-lenses onto semiconductor chips

NILS KOLJA WESSLING,<sup>1</sup>  SAPTARSI GHOSH,<sup>2</sup>  BENOIT GUILHABERT,<sup>1</sup>  MENNO KAPPERS,<sup>2</sup> ALEXANDER M. HINZ,<sup>2,3</sup> MILES TOON,<sup>1</sup> RACHEL A. OLIVER,<sup>2</sup> MARTIN D. DAWSON,<sup>1</sup>  AND MICHAEL J. STRAIN<sup>1,\*</sup> 

<sup>1</sup>*Institute of Photonics, Department of Physics, University of Strathclyde, Glasgow, UK*

<sup>2</sup>*Cambridge Center for Gallium Nitride, University of Cambridge, Cambridge, UK*

<sup>3</sup>*Now at Fraunhofer FEP, Dresden, Germany*

\**michael.strain@strath.ac.uk*

**Abstract:** We demonstrate the back-end integration of optically broadband, high-NA GaN micro-lenses by micro-assembly onto non-native semiconductor substrates. We developed a highly parallel process flow to fabricate and suspend micron scale plano-convex lens platelets from 6" Si growth wafers and show their subsequent transfer-printing integration. A growth process targeted at producing unbowed epitaxial wafers was combined with optimisation of the etching volume in order to produce flat devices for printing. Lens structures were fabricated with 6 – 11  $\mu\text{m}$  diameter, 2  $\mu\text{m}$  height and root-mean-squared surface roughness below 2 nm. The lenses were printed in a vertically coupled geometry on a single crystalline diamond substrate and with  $\mu\text{m}$ -precise placement on a horizontally coupled photonic integrated circuit waveguide facet. Optical performance analysis shows that these lenses could be used to couple to diamond nitrogen vacancy centres at micron scale depths and demonstrates their potential for visible to infrared light-coupling applications.

Published by Optica Publishing Group under the terms of the [Creative Commons Attribution 4.0 License](https://creativecommons.org/licenses/by/4.0/). Further distribution of this work must maintain attribution to the author(s) and the published article's title, journal citation, and DOI.

## 1. Introduction

Micron-sized optical elements are important components for the coupling of light between free-space and matter based systems. Dielectric micro-lens arrays (MLA) are commercially available and commonly used to focus light onto the photon-sensitive regions of CCD [1] and CMOS [2] photo-detector arrays, in order to increase quantum efficiency. Micro-optics are also used to improve the efficiency of light extraction from light emitting diodes (LEDs) [3] and  $\mu$ -LEDs [4], for coupling to integrated photonic circuits (PICs) [5] as well as for improving pump and collection efficiency between microscope systems and semiconductor based solid state quantum emitters [6]. This latter application is particularly challenging due to the often random positioning of the quantum emitters and the large refractive index of the host material that leads to total internal reflection at the interface between the material and free-space.

There are two main routes to fabrication of micro-optics on semiconductor substrates, either additive materials patterning on the substrate, or direct fabrication of optical surfaces into the material itself. There are a number of techniques available for the fabrication of additive components, including imprint lithography [7,8], two-photon polymerization [9–11], thermal reflow [12–14], and inkjet printing [15,16]. Structures formed by these methods are commonly used as the final optical element themselves, but may also be used as a mask for a dry-etch shape transfer into the semiconductor. Two photon polymerization (TPP) is a particularly flexible

method and can be used to fabricate complex micro-optical systems such as multi-lens beam expanders on fibre tips [9] as well as vertical and end-fire couplers to PICs [10,11]. The relatively low refractive index  $n$  of TPP resins ( $n = 1.5 - 1.6$  [17] compared with common semiconductor materials  $n > 2.0$  [18–22]) limits the achievable numerical aperture (NA) of the polymer lenses. Furthermore, polymeric materials are susceptible to catastrophic optical damage at watt-level optical power [10].

Alternatively, solid immersion lenses (SIL) can be formed directly into semiconductor materials by focused ion-beam milling [23,24], laser-micromachining [25,26], photoresist reflow in combination with reactive ion etching [27,28], dual masking [29] and diamond turning [30,31]. These methods make use of the high refractive index of the material itself to avoid refractive index contrast at interface layers, produce high NA performance and are robust to optical damage. Individual lenses can be fabricated with high positional accuracy but require either serial, time consuming processing [23,24], or in the case of diamond substrates are limited in the form factors that can be achieved due to the mask-to-semiconductor etch selectivity [27,28].

In this work, we present an alternative and scalable fabrication scheme, whereby micro-lenses are directly fabricated in GaN material and subsequently transferred to a host chip as membrane devices. The use of a III-N material enables better etch selectivity than in e.g. diamond, while retaining a close refractive index match to semiconductor materials. The devices are fabricated using a combination of grayscale lithography and the photoresist reflow to create spherical photoresist micro-lenses, followed by inductively coupled reactive ion etching (ICP-RIE) to transfer the pattern into a GaN/AlGaIn/AlN layer stack grown on 6" Si wafers [32]. The micro-lenses are suspended over the silicon substrate by wet chemical etching and transferred to

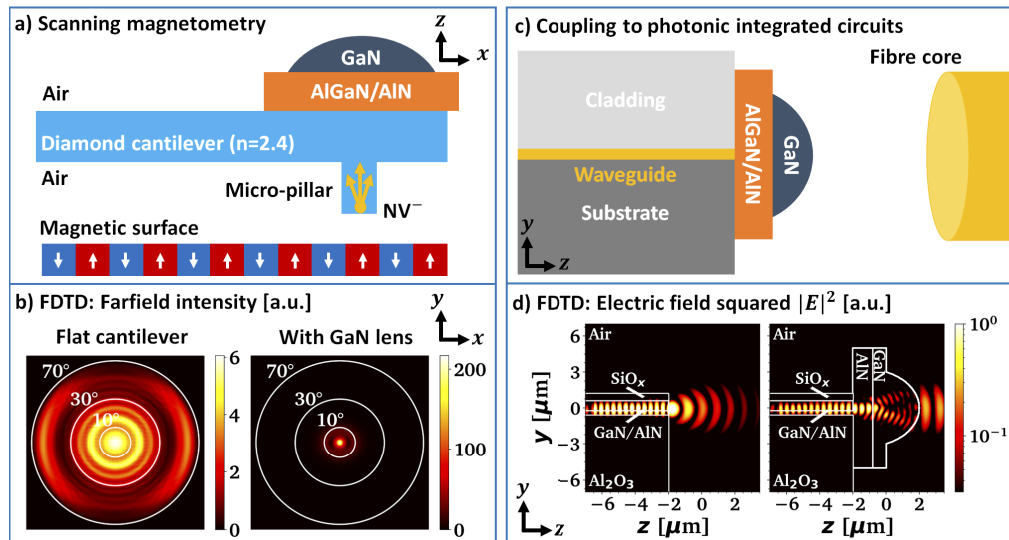


**Fig. 1.** a) Schematic application example for diamond NV scanning magnetometry, exploiting a GaN lens as a light coupler, b) Simulated far field of a dipole emitter placed in a 200 nm wide square micro-pillar (10 nm away from the pillar tip, assuming [111]-orientation) without and with a printed GaN micro-lens (ROC = 16  $\mu\text{m}$ , 15  $\mu\text{m}$  distance to the top of the pillar) at  $\lambda = 650$  nm wavelength c) Schematic of a GaN micro-lens facilitating end-fire coupling between a photonic integrated circuit (left) and a fibre core (right), d) Simulated free-space divergence from the fundamental TE mode of an GaN/AlN waveguide (1.2  $\mu\text{m}$  height, 2  $\mu\text{m}$  width) without and with a GaN micro-lens (ROC = 3.3  $\mu\text{m}$ ) printed on the waveguide facet.

non-native substrates using a transfer printing process. We demonstrate transferred micro-lenses with micron scale radius of curvature (ROC) and focal length  $f$  on diamond substrates. We also show direct printing of a micro-lens onto the facet of a GaN waveguide chip. Two example applications are shown in Fig. 1. In a), light is coupled to and from a diamond nitrogen vacancy ( $NV^-$ ) centre into free-space collection optics for scanning magnetometry [33,34]. By including a GaN micro-lens on the diamond substrate, the effective collection angle from the point emitter is significantly reduced, improving potential coupling efficiency with external, low NA optics and minimising total internal reflection losses. As the minimum detectable magnetic field scales with the square root of the collected fluorescence rate in  $NV^-$  based sensors, the cost of the instrument can be reduced while improving performance metrics such as the measurement acquisition time [35]. More generally, our transfer printing approach leaves the host crystal intact and allows for alignment to randomly positioned quantum emitters. Figure 1(b) shows a scenario where a micro-lens is integrated onto the facet of a GaN/AlN planar waveguide chip, improving modal coupling efficiency between the highly confined on-chip mode and low NA external optics such as a single mode fibre. In both applications, high-NA GaN micro-lenses could potentially substitute other high-NA optical components, while maintaining or improving the system's performance.

## 2. Fabrication and device transfer

Fig. 2 illustrates the process flow for GaN micro-lens fabrication and transfer.

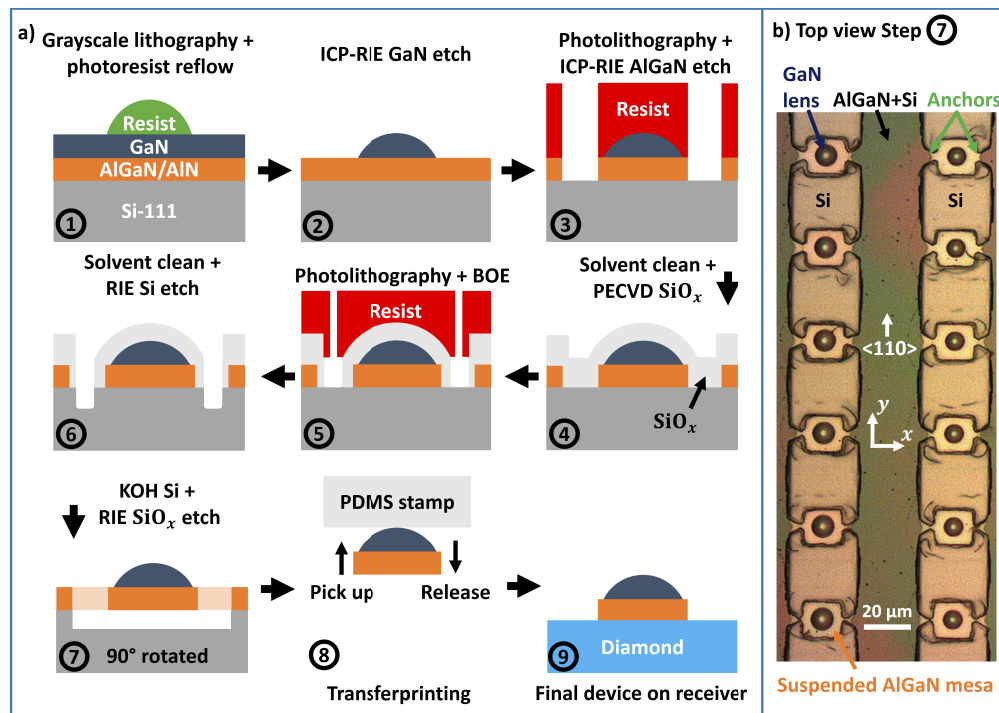


**Fig. 2.** a) Illustration of the process flow after growth, using CVD-grown, single crystalline diamond as receiver substrate, b) Microscope image of a GaN-on-Si donor chip corresponding to process step 6.

A wafer die is spin coated with "Shipley SPR220-4.5" photoresist and micro-lenses are defined in the resist using a combination of grayscale laser lithography (Heidelberg Instruments DWL66+) and thermal reflow on a hotplate at 130-150 °C ①. The grayscale preshaping allows control of

the lens diameter and rounds the resist edges. A step wise increase of the reflow temperature leads to a spherical resist lens with the targeted height and radius of curvature with a smooth surface finish. Alternatively, highly optimised grayscale lithography could be used to directly define the resist profile, with the cost of increased surface roughness. An Ar/Cl<sub>2</sub>-based ICP-RIE (200 W coil power, 70 W platen power, 30 sccm Cl<sub>2</sub>, 10 sccm Ar, 20 mTorr) is used to transfer the lens shape into the GaN ②. The ICP recipe yields etch rates of 200 nm/min for SPR220-4.5 and 150 nm/min for GaN/AlGaN, leading to a selectivity around 0.75. The etch rate drops to around 120 nm/min for AlGaN with Al content  $x > 60\%$  and in the AlN layer. The reactive ion etching results in a lens profile transformation from a spherical resist lens to a parabolic shape of the etched lens, as previously observed in SiC [14], indicating a partly chemical etch and possibly ion channeling effects.

The defined GaN lenses are overlaid with a mesa pattern including suspension anchors using "Shipley SPR220-7.0" photoresist. The previously detailed ICP-RIE recipe is employed to remove the remaining AlGaN and AlN layers, leading to a slight overetch into Si ③. Fig. 2 b) shows a microscope image of already suspended devices, illustrating the etched anchor and mesa pattern defined in this etching step. The 7 μm thick photoresist is needed to successfully protect the GaN lens surface from the plasma, as about 3 μm resist is sacrificed during the etching and the spin coated resist is slightly thinner than the full 7 μm thickness over the protruding lens features.

After resist removal, a conformal layer of 1.8 μm thick SiO<sub>x</sub> is deposited in step ④ by plasma enhanced chemical vapor deposition (PECVD, 70 W RF power, 170 sccm SiH<sub>4</sub>, 710 sccm N<sub>2</sub>O, 1 Torr,  $T = 300\text{ }^{\circ}\text{C}$ ). This hard mask protects the GaN lens from the potassium hydroxide (KOH) wet etch in step ⑤, with thinner layers demonstrating susceptibility to local failure and subsequent chemical etching of the micro-lens features. SPR220-7.0 is used as a lithography mask to open windows at the bottom of the etched trenches and a buffered oxide etch (7:1) removes the SiO<sub>x</sub> with a slight undercut, leaving a sidewall protection layer of SiO<sub>x</sub> on the AlGaN/AlN mesa below the lens ⑤.

An anisotropic RIE etch (100 sccm SF<sub>6</sub>, 8 sccm O<sub>2</sub>, 25 mTorr, 50 W RF-power [36]) is applied after resist removal to etch the Si substrate using the SiO<sub>x</sub> layer as a mask ⑥. The resultant trench allows access for a KOH wet etch solution (40% in weight, 85 °C) to the (110) crystal plane, selectively removing the Si below the lens-mesa along the fast <110> etch direction ⑦. The schematic in Fig. 2 is rotated for this process step, indicating the anchors as semitransparent areas and showing the anisotropic nature of the KOH etch in Si(111). Fig. 2 b) shows a top view. As previously confirmed by scanning transmission electron microscopy [32,37], a nm-thin disordered AlSi<sub>y</sub>N<sub>x</sub> interlayer is formed between Si substrate and AlN nucleation layer, which provides an effective bottom protection against the KOH solution. The smoothness of the mesa bottom surface is confirmed by atomic force microscopy (AFM) measurements after flipping a flat membrane device with a PDMS stamp, yielding 0.4 nm root-mean-squared (r.m.s.) roughness.

The SiO<sub>x</sub> layer is removed by RIE dry etching (5 sccm CHF<sub>3</sub>, 15 sccm Ar, 30 mTorr, 120 W RF-power) to restore the GaN lens surface. AFM surface roughness analysis on a GaN micro-lens after SiO<sub>x</sub> removal showed a surface roughness on the order of 1.4 nm r.m.s.

The suspended micro-lenses are transfer-printed to receiver substrates (single crystalline (SC) diamond or GaN/AlN waveguide facets) using a custom transfer printing system with sub-micron spatial precision [38]. The lenses are removed from their growth substrate using a soft polymer stamp fabricated using a 6:1 ratio Sylgard PDMS with a contact area of 30x30 μm<sup>2</sup> ⑧. The devices are finally aligned to the receiver chip position and released, making use of direct Van-der-Waals interaction between the lens bottom and receiver chip top surface ⑨.

Additional data on the process flow, surface roughness, lens-shape transformation and process yield is given in the supplemental document Fig. S1-5.

### 3. Material growth for membrane flatness

The success of the heterogeneous integration scheme detailed above relies on the flatness of the released membrane devices in addition to the back-side smoothness. If the membrane devices are too bowed, it becomes impossible to achieve a good contact with the receiver substrate, leaving an air cavity between the substrate and the device surface [39,40], which in the case of micro-lens devices can lead to interface reflections and distortion of the desired lens behaviour. Appropriately flat membranes are achieved via careful optimisation of the growth process for the GaN heteroepitaxial layers. The structures used for micro-lens fabrication in this work are grown by metal organic vapor phase epitaxy (MOVPE) on Si(111) substrates. As-grown, the multilayers consist of a  $0.25\ \mu\text{m}$  AlN nucleation layer, a  $1.7\ \mu\text{m}$  graded  $\text{Al}_x\text{Ga}_{1-x}\text{N}$  buffer (with AlN mole fraction  $x$  decreasing from 75% to 25%), and a  $2\ \mu\text{m}$  GaN layer (i.e. a total thickness of ca.  $4\ \mu\text{m}$  nitride material). By successively growing layers with a decreasing Al content, each layer has a slightly larger relaxed lattice constant than that below it, so that the epitaxial growth induces compressive stress. This stress counteracts the post-growth cooldown related tensile stress originating from the thermal expansion mismatch between the silicon substrate and the nitride epitaxial layers. Post-growth, the wafer-bow is a function of the residual stresses and thickness of the individual epilayers. For a membrane released from the growth substrates, its deflection is also dependent on these in-built stresses in the remaining layers and related to the wafer bow [41].

The wafer bow can be controlled by exposing the substrate to ammonia at  $1000\ ^\circ\text{C}$  prior to deposition of the AlN nucleation layer. By changing the duration of the ammonia pre-dose, the bow may be tuned from convex to concave. Initial trials of the membrane fabrication process with the pre-dose duration varying (without any lens fabrication) used a series of wafers in which a  $1\ \mu\text{m}$  GaN epilayer was grown on top of similar underlying buffer layers to those employed for the micro-lens fabrication. These trials indicated that minimising the wafer bow also yielded the least bowed membrane (see supplemental document, Fig. S6). Based on this information, for the present studies with  $2\ \mu\text{m}$  thick GaN layers, material from two nearly-flat wafers (having respective bow values of  $+7\ \mu\text{m}$  and  $-2\ \mu\text{m}$ ) are used for the experiments. It is observed that even for material from flat wafers, the material removal in the micro-lens fabrication needs to be further optimised to realise flat devices.

For example, Fig. 3 a) shows a test membrane with a planar surface (i.e. no lens topology) where material was removed by ICP-RIE until  $1.2\ \mu\text{m}$  of the combined graded AlGa<sub>x</sub>N buffer and AlN nucleation layer remained. Though the source wafer had near-zero bow, when the resulting AlGa<sub>x</sub>N/AlN membrane is transferred to a diamond substrate, a clear interference fringe pattern appears. This indicates an air gap below the device. An AFM scan confirms convex bowing of the membrane, showing that the maximum width of the air gap is on the order of 250 nm.

Membranes with micro-lens topology are also bowed when etched to this same remaining thickness of  $1.2\ \mu\text{m}$ , as shown in Fig. 3 b). However, the effect is observed to be most pronounced for the smallest micro-lens whose colour fringes closely resemble the planar membrane device in Fig. 3 a). As the lens diameter increases, the coloured fringes decrease in spatial frequency, indicating a reduced membrane bow. This can be explained by the fact that in membranes where the original layer thicknesses are maintained, the summation of bending moments arising from each layer are balanced. Once the thicknesses and/or volumes are altered (e.g. by partial etching of the layers to create a lens geometry), this balance is disrupted, so that the membrane starts to bow, creating an additional bending stress restoring equilibrium. This effect is here further enhanced, since lens height and the diameter are for these particular devices positively correlated, with the height rising from  $2\ \mu\text{m}$  to  $3\ \mu\text{m}$ , compare Fig. S7 for AFM data. As more material is removed, like in the case of small radius of curvature lens structures, the bow of the devices becomes larger. Hence, the optimised micro-lenses are designed to leave more of the epitaxial stack intact by limiting the lens etch depth to  $2\ \mu\text{m}$ , matching the thickness of the GaN epilayer.

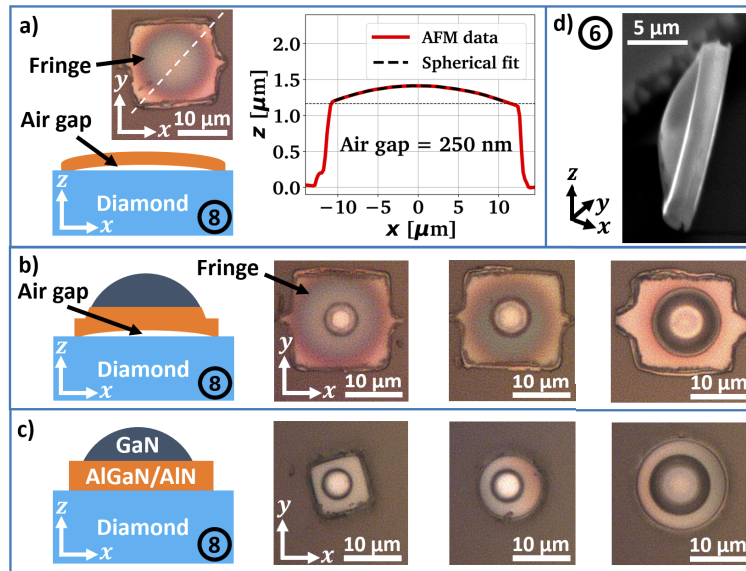


**Fig. 3.** a) Schematic, microscope image and AFM analysis of a  $1.2\ \mu\text{m}$  thin AlGaIn membrane transfer printed onto SC diamond, b)/c) Schematic and microscope images of  $2 - 3\ \mu\text{m}$  high micro-lenses in b) on bowed,  $1.2\ \mu\text{m}$  thick mesas with anchors and in c) on flat,  $2\ \mu\text{m}$  thick mesas without anchors printed on SC diamond, d)  $40^\circ$  tilted SEM image of a  $2\ \mu\text{m}$  high GaN lens with a flat,  $2\ \mu\text{m}$  thick mesa standing on the donor substrate.

As shown in Fig. 3 c), this balanced height of GaN micro-lens and AlGaIn/AlN mesa did not result in air cavity induced colour fringes after the transfer step. The flatness of these membranes can be further confirmed by the tilted SEM image in Fig. 3 d) which shows a micro-lens membrane from a side-view.

Fig. 4 a) shows SEM images of devices without anchoring tethers collapsed to the Si surface after KOH etch and  $\text{SiO}_x$  mask removal. For optical testing, we selected three similar micro-lenses with varying diameter (①, ②, ③) printed on a electronic grade single crystalline CVD diamond membrane from Element6 [ $2 \times 2\ \text{mm}^2$ ,  $N < 5\ \text{ppb}$ ], see Fig. 4 b) for microscope images. AFM profile scans of these devices are plotted in c) and fitted both with a spherical and parabolic function. Both fits match the data well, but the parabolic fit performs slightly better, showing r.m.s. deviation from the data of 30, 35 and 55 nm compared to 40, 60 and 105 nm for the spherical fit, ordered left to right according to device ①, ② and ③. The Maréchal criterion defines an optical focussing system as diffraction limited when the r.m.s. wavefront error is smaller than  $\lambda/14$  across the full aperture [42]. For a wavelength of  $\lambda = 650\ \text{nm}$ , this corresponds to roughly 33 nm r.m.s. surface deviation (weighted by the index contrast  $n - 1$ ). Devices ① and ② show surface variations from the spherical and parabolic fit close to this threshold, so we do not expect significant loss of optical performance. The smallest micro-lens, device ③, shows reasonable agreement with the parabolic shape, which should make it effective at collimating light from its focal position close to the diamond surface.

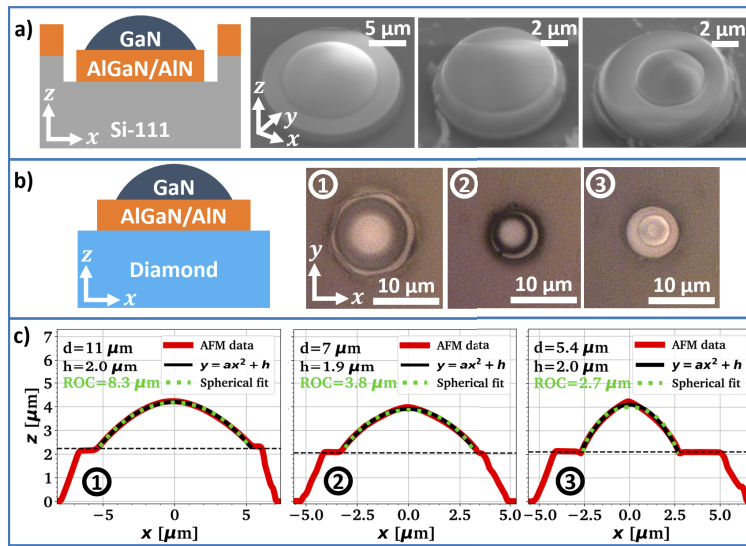


**Fig. 4.** a) Schematic and  $40^\circ$  tilted SEM images of collapsed micro-lenses on membranes without anchors on the donor substrate, b) Schematic and microscope image of the transfer-printed devices on SC diamond used for the optical analysis in Fig. 6, c) AFM topography and shape analysis of the devices shown in b), with lens diameter  $d$ , height  $h$  and ROC extracted from the correspondingly colored fit.

#### 4. Optical analysis

The focal lengths of the three lenses printed onto a SC diamond substrate, shown in Fig. 4 b)/c), are measured using a custom built infinity-corrected microscope illustrated in Fig. 5, which is based on [43]. The light from a tungsten lamp (Ocean optics HL-2000-FHSA) is collimated with a convex lens (CL) and passed through a colour filter (CF) primarily transmitting green light. For additional spectral selection, only the green pixel channel of the CCD colour camera with a Bayer filter (Allied Vision Prosilica GC650-C) is used for the analysis, leading to a total of 10 dB rejection in the  $\lambda = 525 \pm 50$  nm wavelength range. The measured transmission spectrum of the setup is shown in Fig. S8 in the supplementary document. The refractive index of GaN varies only by ca. 2% in this wavelength range [21]. The collimated beam is coupled through the back-side of the diamond substrate and then through the printed GaN micro-lenses on the opposite face. The wide field illumination allows imaging of the micro-lenses with an infinity-corrected 60x objective (Nikon Plan Fluor, NA = 0.85), using a 200 mm tube lens (TL, Thorlabs LA1708-A) to image onto a CCD array. A calibrated piezo controller (PI P-725.4CD with E-665CR) is used to manipulate the objective's  $z$ -position with sub-micron accuracy. Automated  $z$ -scans are constructed by taking images in synchronisation with the piezo position.

The focal length  $f_{air}$  of the micro-lens in air is extracted from the  $z$ -scan as a bright spot on the CCD camera, when the focal spot of the objective and micro-lens overlap. We then compare the  $z$ -travel distance between a sharp image of the micro-lens mesa and the image of the focal spot to extract  $f_{air}$ . The broadband source was used in these measurements to avoid the obscuring interference fringes generated by monochromatic sources.

The expected focal length of the three example micro-lenses is calculated using 3D FDTD simulations (Lumerical) in which the lenses are created to match the form factor of the measured devices, based on the AFM profiles, as shown in Fig. 4 c). The refractive index model for the micro-lens structure is based on [20–22,45], using  $\text{Al}_x\text{Ga}_{1-x}\text{N}$  with  $x = 38\%$ .

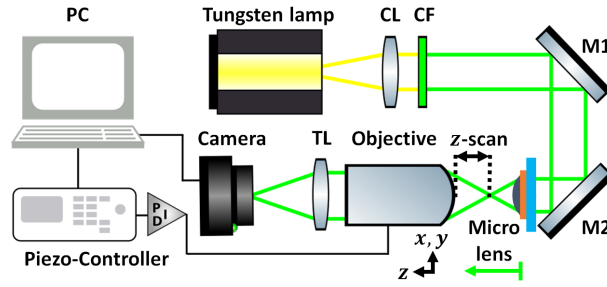


**Fig. 5.** Optical setup used to evaluate the focal length of GaN micro-lenses printed onto diamond, based on [43]. The convex lens CL, green colour filter CF, mirrors M1 and M2 and tube lens TL are annotated. Illustrations are taken from [44].

Fig. 6 a) shows the simulated electric field strength squared for a plane wave injected from the diamond substrate upwards through the micro-lens geometry at  $\lambda = 525$  nm wavelength. We chose the apparent symmetry point of the focal spot to evaluate the focal length  $f_{air}$  measured from the GaN micro-lens tip. The results are displayed in Tab. 1 and compared to what would be expected from the geometric optics (GO) approximation for a spherical surface with index  $n_{\text{GaN},\lambda=525\text{ nm}} = 2.43$  [21] (compared to  $n_{\text{dia},\lambda=525\text{ nm}} = 2.43$  [20]). We evaluate the following equations [46] with the lens diameter  $d$  and height  $h$  found in the spherical fit in Fig. 4 c):

$$\text{ROC} = \frac{\left(\frac{d}{2}\right)^2 + h^2}{2h} \quad f_{air} = \text{ROC} \cdot \frac{1}{n_{\text{GaN},\lambda=525\text{ nm}} - 1}$$

The shortened focal lengths found in the FDTD simulations in comparison to the GO approximation shows the necessity to use a full Maxwell solver to accurately predict the micro-lens performance. The diffraction effect evident in the simulations is known as focal shift and is well documented for small scale micro-optics [47–49]. Diffraction is also reported to account for the visible "funneling" of light into a tube, rather than a distinct focal spot [47], and can be seen in Fig. 6 a).

**Table 1. Results of the AFM and optical analysis of the lenses shown in Fig. 4 b)/c). Diameter  $d$ , height  $h$ , radius of curvature (ROC) and focal length  $f$  are given for the geometric optics (GO) approximation and FDTD simulations and compared to the experimental data (EXP).  $f_{air}$  is simulated at  $\lambda = 525$  nm, while  $f_{dia}$  is simulated at  $\lambda = 700$  nm wavelength.**

	$d$	$h$	ROC	$f_{air}$ GO	$f_{air}$ FDTD	$f_{air}$ EXP	$f_{dia}$ FDTD	$\text{NA}_{dia}$
		[ $\mu\text{m}$ ]	[ $\mu\text{m}$ ]	[ $\mu\text{m}$ ]	[ $\mu\text{m}$ ]	[ $\mu\text{m}$ ]	[ $\mu\text{m}$ ]	[ $\mu\text{m}$ ]
①	11	2.0	8	6	4	$4.5 \pm 1.0$	14	1.0
②	7	1.9	4	3	2	$2.0 \pm 1.0$	7	1.4
③	5.5	2.0	3	2	1	$1.5 \pm 1.0$	5	1.7

Fig. 6 b) shows the measured  $z$ -scan sections with  $0.5 \mu\text{m}$  step size for each micro-lens. The lens geometries from the FDTD simulations are overlaid as a guide to the eye, with their locations defined by imaging the mesa structures. The measured position of the focal point is extracted as the highest intensity spot above the lens surface in air and is presented alongside the simulation values in Tab. 1. The measurement errors are dominated by the uncertainty regarding the lens surface position (found from the  $z$ -position of the mesa image) and the  $\mu\text{m}$ -large measured depth of focus in the measurement setup.



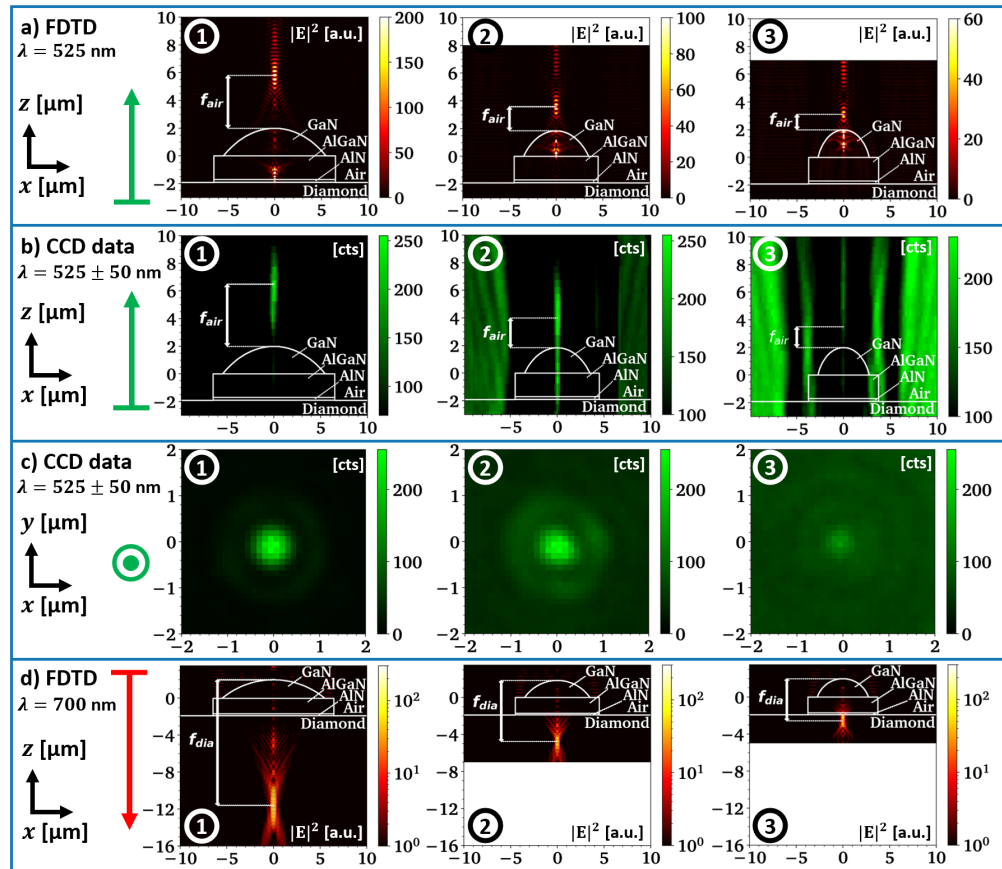


**Fig. 6.** Optical analysis of the GaN micro-lenses on diamond shown in Fig. 4 b/c): a) FDTD simulations of the electric field squared with a linearly polarised plane wave injected at  $\lambda = 525 \text{ nm}$  wavelength from diamond through spherical lens profiles, b) Measured  $z$ -scan of the  $x$ -profile through the  $xy$ -CCD data evaluated on the lenses with the setup shown in Fig. 5, overlaid with contours from the FDTD simulations in a), c)  $xy$ -CCD data at the objective's focal position matching  $f_{air}$  in b), d) FDTD simulations of the electric field squared with a linearly polarised plane wave injected at  $\lambda = 700 \text{ nm}$  from air into the indicated spherical micro-lenses on diamond.

The  $xy$ -view of the selected focal spot is shown in Fig. 6 c). The full-width-half-maximum (FWHM) of the measured focal spot size is on the order of 700 – 800 nm, showing reasonable circular symmetry. We do not expect to reach the diffraction limited spot size (FWHM  $\approx$  500 – 750 nm for  $\lambda = 525$  nm and simulated NA in air of  $\approx$  0.5, 0.4 and 0.35 for devices ①, ② and ③, respectively [43]) as we use a broadband beam with low coherence.

Expected and measured focal lengths agree well for lenses ① and ②, but the results for the highest-aspect ratio micro-lens ③ are more challenging to extract due to the lack of a clear signature of the focal spot. This may be partially due to the reduction of contrast due to the decreasing lens aperture, which is additionally masked by increasing total internal reflections when transitioning to a higher aspect ratio lens. This loss of contrast is visible in Fig. 6 c). Spherical aberration and astigmatism might also lead to a wider spread of the focus along the  $z$ -axis.

Due to the substrate thickness and high index contrast, it is experimentally challenging to measure the focal length  $f_{dia}$  of the micro-lenses in diamond. But as there is overall reasonable agreement between measured results and FDTD simulations,  $f_{dia}$  can be estimated by inverting the FDTD simulations, see Fig. 6 d). In this case, a linearly polarised plane wave is injected from the top of the sample through the lens and into the substrate. Here we use  $\lambda = 700$  nm wavelength corresponding to the central wavelength of  $NV^-$  emission at room temperature [50], with  $n_{GaN, \lambda=700\text{ nm}} = 2.37$  [21] and  $n_{dia, \lambda=700\text{ nm}} = 2.41$  [20]. The focal length  $f_{dia}$  in diamond in reference to the GaN lens tip is assessed by identifying the symmetry point of the apparent focal spot, which leads to the results presented in Tab. 1. These values imply that the fabricated micro-lenses could be used to couple to  $NV^-$  centres both in nm-proximity to the diamond surface and in up to 10  $\mu\text{m}$  depth. To illustrate the light collection potential of our demonstrated micro-lenses, we calculate the numerical aperture for collection from diamond using the following expression:

$$NA_{dia} = n_{dia} \cdot \sin \left( \arctan \left( \frac{d}{2(f_{dia} - h)} \right) \right)$$

which indicates potentially comparable performance to high-end oil immersion objectives.

## 5. Printed GaN micro-lens on a waveguide facet

To show the compatibility of the free-standing micro-lens transfer with challenging device geometries, we integrated a high-aspect ratio micro-lens onto the polished facet of a straight waveguide on a GaN-on-sapphire PIC with a 600 nm thin  $\text{SiO}_2$  upper-cladding layer. The GaN/AlN waveguides have a total thickness of 1.2  $\mu\text{m}$ , with 850 nm GaN on top of a 350 nm AlN nucleation layer. The waveguide width is 2  $\mu\text{m}$  at the facet, but is tapered down to 1  $\mu\text{m}$  on the chip. See Fig. 1 d) for the corresponding FDTD simulation.

A tilted SEM image of the micro-lens is shown in Fig. 7 a), while microscope images of the facet before and after printing are shown in b), including an overlay of images before and after printing in the center. The chip did not contain any local alignment markers to guide a print on the facet, which restricted the alignment accuracy to around  $\pm 1 \mu\text{m}$ . The cladding layer is very thin, which causes roughly a third of the micro-lens to remain suspended in air, demonstrating the versatility of the approach and the flatness of the printed device. As previous work has shown nm-scale accuracy with transfer printing [38], alignment to a chip with dedicated markers and a thicker cladding layer should allow printing accuracy with sub-micron precision.

We imaged the light output from the waveguide facet through the micro-lens using a 60x objective with a 500 mm tube lens to reach 150x magnification. The output mode at  $\lambda = 1630$  nm wavelength is shown in Fig. 7 c), indicating the transparency of the lens in this wavelength region. The top view image in Fig. 7 d) shows the lens after optical characterisation, validating the mechanical stability of the bond between lens and the polished facet even with the limited bond area.

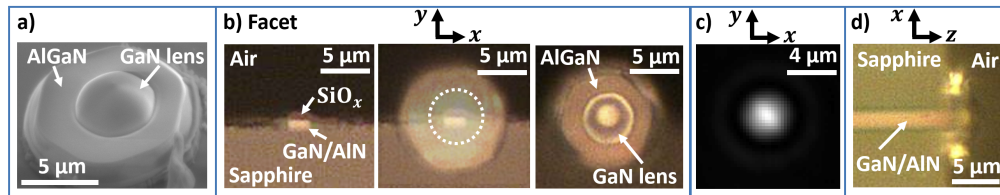


**Fig. 7.** High-aspect ratio GaN micro-lens printed on GaN-on-sapphire waveguide facet. a)  $40^\circ$  tilted SEM image of the micro-lens on the donor sample, b) Microscope images of the waveguide facet ( $1.2 \times 2 \mu\text{m}^2$ ) before (left) and after (right) transfer printing, the centre image shows an overlay, c) Imaged output mode from the waveguide with printed micro-lens at  $\lambda = 1630 \text{ nm}$  wavelength at 150x magnification, d) Top view of the printed lens after mode imaging.

## 6. Conclusion and Outlook

Gallium nitride is an attractive material for micro-lens fabrication due to its broad optical transparency, high refractive index and ready availability in epistructure format. Here, we have demonstrated the dry transfer of such GaN micro-lenses fabricated from GaN-on-Si, permitting back-end integration in an additive process for a range of applications. Importantly, this approach offers deterministic positioning of the micro-lenses and avoids the risk of fabrication induced damage to solid state quantum emitters in monolithic fabrication approaches. Additionally, the dry etch based fabrication and wafer-scale availability of GaN-on-Si potentially enables scaling the process flow.

Careful optimisation of the growth and fabrication steps enables direct contact printing of flat membrane devices onto semiconductor substrates, here demonstrated using CVD-grown single crystalline diamond as a receiver. The etch depth of the micro-lenses strongly affects the released device flatness, highlighting the interplay between material stress profile and etch geometry. The lens imaging measurements on the diamond substrate show good agreement with FDTD simulations, which are compatible with schemes for efficient coupling to diamond  $\text{NV}^-$  centres at a range of 0.1 to  $10 \mu\text{m}$  depth from the material surface.

Additionally, we printed a GaN lens on a GaN/AlN waveguide facet, showing compatibility of additive micro-optics with  $\mu\text{m}$ -precision transfer, even when partially suspended in air. The print demonstrates both the flatness of our devices and the flexibility of the transfer-printing approach for end-fire coupling.

Future work aims to demonstrate light collection from colour centres in diamond and other high index materials such as GaN [51] or SiC [52] and efficient coupling to photonic integrated circuits in the VIS and NIR wavelength regime. Using highly optimised grayscale lithography, the benefits of free-form optics can be added to the developed additive GaN micro-optics platform.

**Funding.** Royal Academy of Engineering (Research Chairs, Senior Research Fellowships); Engineering and Physical Sciences Research Council (EP/N017927/1, EP/P00945X/1, EP/R03480X/1); Innovate UK (50414); Fraunhofer Lighthouse Project Qmag; NKW acknowledges funding of his PhD studentship by Fraunhofer UK.

**Acknowledgments.** The authors thank Jack Smith for providing the GaN-on-sapphire photonic integrated circuit chip, which was partially fabricated in the James Watt Nanofabrication center at the University of Glasgow.

**Disclosures.** The authors declare no conflicts of interest.

**Data availability.** Data underlying the results presented in this paper are available in Ref. [53].

**Supplemental document.** See Supplement 1 for supporting content.

## References

1. R. Stevens and T. Miyashita, "Review of standards for microlenses and microlens arrays," *The Imaging Sci. J.* **58**(4), 202–212 (2010).

2. J. E. G. Douglas A. Baillie, "Zero-space microlenses for CMOS image sensors: optical modeling and lithographic process development," *Proc. SPIE* **5377**, 953–959 (2004).
3. A. Braeuer, P. Dannberg, U. Zeitner, G. Mann, and W. Karthe, "Application oriented complex polymer microoptics," *Microsyst. Technol.* **9**(5), 304–307 (2003).
4. H. W. Choi, E. Gu, J. M. Girkin, and M. D. Dawson, "Nitride micro-display with integrated micro-lenses," *phys. stat. sol. (c)* **2**(7), 2903–2906 (2005).
5. R. Marchetti, C. Lacava, L. Carroll, K. Gradkowski, and P. Minzioni, "Coupling strategies for silicon photonics integrated chips [Invited]," *Photonics Res.* **7**(2), 201 (2019).
6. A. Bogucki, L. Zinkiewicz, M. Grzeszczyk, W. Pacuski, K. Nogajewski, T. Kazmierczuk, A. Rodek, J. Suffczyński, K. Watanabe, T. Taniguchi, P. Wasylczyk, M. Potemski, and P. Kossacki, "Ultra-long-working-distance spectroscopy of single nanostructures with aspherical solid immersion microlenses," *Light: Sci. Appl.* **9**(1), 48 (2020).
7. R. Voelkel, "Wafer-scale micro-optics fabrication," *Adv. Opt. Technol.* **1**(3), 135–150 (2012).
8. A. R. Moharana, H. M. Außerhuber, T. Mitteramskogler, M. J. Haslinger, and M. M. Mühlberger, "Multilayer nanoimprinting to create hierarchical stamp masters for nanoimprinting of optical micro-and nanostructures," *Coatings* **10**(3), 301 (2020).
9. T. Gissibl, S. Thiele, A. Herkommer, and H. Giessen, "Two-photon direct laser writing of ultracompact multi-lens objectives," *Nat. Photonics* **10**(8), 554–560 (2016).
10. P. I. Dietrich, M. Blaicher, I. Reuter, M. Billah, T. Hoose, A. Hofmann, C. Caer, R. Dangel, B. Offrein, U. Troppenz, M. Moehrl, W. Freude, and C. Koos, "In situ 3D nanoprinting of free-form coupling elements for hybrid photonic integration," *Nat. Photonics* **12**(4), 241–247 (2018).
11. H. Gehring, A. Eich, C. Schuck, and W. H. P. Pernice, "Broadband out-of-plane coupling at visible wavelengths," *Opt. Lett.* **44**(20), 5089 (2019).
12. T. N. Oder, J. Shakya, J. Y. Lin, and H. X. Jiang, "Nitride microlens arrays for blue and ultraviolet wavelength applications," *Appl. Phys. Lett.* **82**(21), 3692–3694 (2003).
13. H. W. Choi, E. Gu, C. Liu, C. Griffin, J. M. Girkin, I. M. Watson, and M. D. Dawson, "Fabrication of natural diamond microlenses by plasma etching," *J. Vac. Sci. Technol. B* **23**(1), 130–132 (2005).
14. F. Sardi, T. Kornher, M. Widmann, R. Kolesov, F. Schiller, T. Reindl, M. Hagel, and J. Wrachtrup, "Scalable production of solid-immersion lenses for quantum emitters in silicon carbide," *Appl. Phys. Lett.* **117**(2), 022105 (2020).
15. A. Zolfaghari, T. Chen, and A. Y. Yi, "Additive manufacturing of precision optics at micro and nanoscale," *Int. J. Extrem. Manuf.* **1**(1), 012005 (2019).
16. A. C. Fischer, M. Mäntysalo, and F. Niklaus, "Inkjet printing, laser-based micromachining, and micro–3D printing technologies for MEMS," in *Handbook of Silicon Based MEMS Materials and Technologies*, (2020), pp. 531–545.
17. NanoScribe GmbH & Co. KG, <https://www.nanoscribe.com/en/products/ip-resins>, (2022).
18. M. A. Green, "Self-consistent optical parameters of intrinsic silicon at 300 K including temperature coefficients," *Solar Energy Materials and Solar Cells* **92**(11), 1305–1310 (2008).
19. C. Xu, S. Wang, G. Wang, J. Liang, S. Wang, L. Bai, J. Yang, and X. Chen, "Temperature dependence of refractive indices for 4H- and 6H-SiC," *J. Appl. Phys.* **115**(11), 113501 (2014).
20. H. R. Phillip and E. A. Taft, "Kramers-Kronig analysis of reflectance data for diamond," *Phys. Rev.* **136**(5A), A1445–A1448 (1964).
21. A. S. Barker and M. Ilegems, "Infrared lattice vibrations and free-electron dispersion in GaN," *Phys. Rev. B* **7**(2), 743–750 (1973).
22. J. Pastrňák and L. Roskocova, "Refraction index measurements on AlN single crystals," *phys. stat. sol. (b)* **14**(1), K5–K8 (1966).
23. L. Marseglia, J. P. Hadden, A. C. Stanley-Clarke, J. P. Harrison, B. Patton, Y. L. Ho, B. Naydenov, F. Jelezko, J. Meijer, P. R. Dolan, J. M. Smith, J. G. Rarity, and J. L. O'Brien, "Nanofabricated solid immersion lenses registered to single emitters in diamond," *Appl. Phys. Lett.* **98**(13), 133107 (2011).
24. M. Jamali, I. Gerhardt, M. Rezai, K. Frenner, H. Fedder, and J. Wrachtrup, "Microscopic diamond solid-immersion-lenses fabricated around single defect centers by focused ion beam milling," *Rev. Sci. Instrum.* **85**(12), 123703 (2014).
25. H. M. Presby, A. F. Benner, and C. A. Edwards, "Laser micromachining of efficient fiber microlenses," *Appl. Opt.* **29**(18), 2692 (1990).
26. B. Hao, H. Liu, F. Chen, Q. Yang, P. Qu, G. Du, J. Si, X. Wang, and X. Hou, "Versatile route to gapless microlens arrays using laser-tunable wet-etched curved surfaces," *Opt. Express* **20**(12), 12939 (2012).
27. E. Gu, H. W. Choi, C. Liu, C. Griffin, J. M. Girkin, I. M. Watson, M. D. Dawson, G. McConnell, and A. M. Gurney, "Reflection/transmission confocal microscopy characterization of single-crystal diamond microlens arrays," *Appl. Phys. Lett.* **84**(15), 2754–2756 (2004).
28. C. L. Lee, E. Gu, M. D. Dawson, I. Friel, and G. A. Scarsbrook, "Etching and micro-optics fabrication in diamond using chlorine-based inductively-coupled plasma," *Diamond Relat. Mater.* **17**(7–10), 1292–1296 (2008).
29. Y. Zhang, Y. Li, L. Liu, C. Yang, Y. Chen, and S. Yu, "Demonstration of diamond microlens structures by a three-dimensional (3D) dual-mask method," *Opt. Express* **25**(13), 15572 (2017).
30. S. To, Z. Zhu, and H. Wang, "Virtual spindle based tool servo diamond turning of discontinuously structured microoptics arrays," *CIRP Annals* **65**(1), 475–478 (2016).

31. M. Mukaida and J. Yan, "Fabrication of hexagonal microlens arrays on single-crystal silicon using the tool-servo driven segment turning method," *Micromachines* **8**(11), 323 (2017).
32. S. Ghosh, A. Hinz, S. M. Fairclough, B. F. Spiridon, A. Eblabla, M. A. Casbon, M. J. Kappers, K. Elgaid, S. Alam, R. A. Oliver, and D. J. Wallis, "Origin(s) of anomalous substrate conduction in MOVPE-grown GaN HEMTs on highly resistive silicon," *ACS Appl. Electron. Mater.* **3**(2), 813–824 (2021).
33. G. Balasubramanian, I. Y. Chan, R. Kolesov, M. Al-Hmoud, J. Tisler, C. Shin, C. Kim, A. Wojcik, P. R. Hemmer, A. Krueger, T. Hanke, A. Leitenstorfer, R. Bratschitsch, F. Jelezko, and J. Wrachtrup, "Nanoscale imaging magnetometry with diamond spins under ambient conditions," *Nature* **455**(7213), 648–651 (2008).
34. P. Maletinsky, S. Hong, M. S. Grinolds, B. Hausmann, M. D. Lukin, R. L. Walsworth, M. Loncar, and A. Yacoby, "A robust scanning diamond sensor for nanoscale imaging with single nitrogen-vacancy centres," *Nat. Nanotechnol.* **7**(5), 320–324 (2012).
35. J. M. Taylor, P. Cappellaro, L. Childress, L. Jiang, D. Budker, P. Hemmer, A. Yacoby, R. Walsworth, and M. Lukin, "High-sensitivity diamond magnetometer with nanoscale resolution," *Nat. Phys.* **4**(10), 810–816 (2008).
36. K. A. Shaw, Z. L. Zhang, and N. C. MacDonald, "SCREAM I: A single mask, single-crystal silicon, reactive ion etching process for microelectromechanical structures," *Sens. Actuators, A* **40**(1), 63–70 (1994).
37. S. Fairclough, A. Hinz, S. Ghosh, B. Spiridon, D. Wallis, and R. Oliver, "Direct evidence of an Al alloyed SiNx interlayer within an ammonia predeposited Al/Si interface via STEM-EELS," in *Proceedings of Electron Beam Spectroscopy for Nanooptics 2021 (EBSN2021)*, (2021).
38. J. McPhillimy, D. Jevtics, B. J. E. Guilhabert, C. Klitis, A. Hurtado, M. Sorel, M. D. Dawson, and M. J. Strain, "Automated Nanoscale Absolute Accuracy Alignment System for Transfer Printing," *ACS Appl. Nano Mater.* **3**(10), 10326–10332 (2020).
39. Z. Shaban, Z. Li, B. Roycroft, M. Saei, T. Mondal, and B. Corbett, "Transfer printing of roughened GaN "based light" emitting diodes into reflective trenches for visible light communication," *Adv. Photonics Res.* **3**(8), 2100312 (2022).
40. A. J. Trindade, B. Guilhabert, E. Y. Xie, R. Ferreira, J. J. D. McKendry, D. Zhu, N. Laurand, E. Gu, D. J. Wallis, I. M. Watson, C. J. Humphreys, and M. D. Dawson, "Heterogeneous integration of gallium nitride light-emitting diodes on diamond and silica by transfer printing," *Opt. Express* **23**(7), 9329 (2015).
41. B. F. Spiridon, M. Toon, A. Hinz, S. Ghosh, S. M. Fairclough, B. J. E. Guilhabert, M. J. Strain, I. M. Watson, M. D. Dawson, D. J. Wallis, and R. A. Oliver, "Method for inferring the mechanical strain of GaN-on-Si epitaxial layers using optical profilometry and finite element analysis," *Opt. Mater. Express* **11**(6), 1643 (2021).
42. H. Ottevaere, R. Cox, H.-P. Herzig, T. Miyashita, K. Naessens, M. Taghizadeh, R. Völkel, H. Woo, and H. Thienpont, "Comparing glass and plastic refractive microlenses fabricated with different technologies," *J. Opt. A: Pure Appl. Opt.* **8**(7), S407–S429 (2006).
43. M. Baranski, S. Perrin, N. Passilly, L. Froehly, J. Albero, S. Bargiel, and C. Gorecki, "A simple method for quality evaluation of micro-optical components based on 3D IPSF measurement," *Opt. Express* **22**(11), 13202 (2014).
44. A. Franzen, <http://www.gwoptics.org/ComponentLibrary/>, (2022).
45. G. M. Laws, E. C. Larkins, I. Harrison, C. Molloy, and D. Somerford, "Improved refractive index formulas for the Al<sub>x</sub>Ga<sub>1-x</sub>N and In<sub>y</sub>Ga<sub>1-y</sub>N alloys," *J. Appl. Phys.* **89**(2), 1108–1115 (2001).
46. W. Demtröder, *Experimentalphysik 2 - Elektrizität und Optik*, vol. 5 (2009).
47. P. Nussbaum, R. Völkel, H. P. Herzig, M. Eisner, and S. Haselbeck, "Design, fabrication and testing of microlens arrays for sensors and microsystems," *Pure Appl. Opt.* **6**, 617–636 (1997).
48. M.-S. Kim, T. Scharf, and H. P. Herzig, "Small-size microlens characterization by multiwavelength high-resolution interference microscopy," *Opt. Express* **18**(14), 14319 (2010).
49. G. J. Lee, H. M. Kim, and Y. M. Song, "Design and fabrication of microscale, thin-film silicon solid immersion lenses for mid-infrared application," *Micromachines* **11**(3), 250 (2020).
50. A. Gruber, A. Dräbenstedt, C. Tietz, L. Fleury, J. Wrachtrup, and C. Von Borczyskowski, "Scanning confocal optical microscopy and magnetic resonance on single defect centers," *Science* **276**(5321), 2012–2014 (1997).
51. A. M. Berhane, K. Y. Jeong, Z. Bodrog, S. Fiedler, T. Schröder, N. V. Trivino, T. Palacios, A. Gali, M. Toth, D. Englund, and I. Aharonovich, "Bright room-temperature single-photon emission from defects in gallium nitride," *Adv. Mater.* **29**(12), 1605092 (2017).
52. C. P. Anderson, E. O. Glen, C. Zeledon, A. Bourassa, Y. Jin, Y. Zhu, C. Vorwerk, A. L. Crook, H. Abe, J. Ul-Hassan, T. Ohshima, N. T. Son, G. Galli, and D. D. Awschalom, "Five-second coherence of a single spin with single-shot readout in silicon carbide," *Sci. Adv.* **8**(5), 1 (2022).
53. N. K. Wessling, S. Ghosh, B. Guilhabert, M. Kappers, A. M. Hinz, M. Toon, R. A. Oliver, M. D. Dawson, and M. J. Strain, "Data for: "Fabrication and transfer printing based integration of free-standing GaN membrane micro-lenses onto semiconductor chips";" University of Strathclyde, 2022, <https://doi.org/10.15129/1352ed1d-5b90-4b7f-9541-a9dcffe1d275>.